

# Visualization and Simulation of the Transfer Process of Index-Matched Silica Microparticle Inks for Gravure Printing

Arnout M. P. Boelens and Juan J. de Pablo

Institute for Molecular Engineering, University of Chicago, Chicago, IL 60637

Sooman Lim and Lorraine Francis

Dept. of Chemical Engineering and Material Science, University of Minnesota, Minneapolis, MN 55455

Bok Y. Ahn and Jennifer A. Lewis

Harvard John A. Paulson School of Engineering and Applied Sciences, Cambridge, MA 02138

DOI 10.1002/aic.15392

Published online in Wiley Online Library (wileyonlinelibrary.com)

*A combined experimental and computational study of the transfer of transparent index-matched silica-particle inks between two flat plates is presented for gravure printing applications. The influence of printing speed and initial ink droplet size on the ability to accurately transfer ink during the printing process is explored systematically. Smooth interface volume of fluid simulations show the same trends as the ink transfer observed in experiments over a wide range of printing speeds and for inks having different silica particle loadings. Our calculations indicate that for ink droplets with characteristic dimensions in the vicinity of 10  $\mu\text{m}$ , which are of particular interest for gravure printing applications, ink transfer improves significantly due to the diminishing effect of gravity, and the increased importance of capillary forces at small length scales. © 2016 American Institute of Chemical Engineers AICHE J, 00: 000–000, 2016*

*Keywords: fluid mechanics, computational fluid dynamics, microfluidics, rheology, materials*

## Introduction

Gravure printing is commonly used for coating and printing processes. It represents an example of a free-surface flow<sup>1–9</sup> or, more specifically, of a liquid-bridge problem. A recent, renewed interest in gravure printing has been motivated by the search for viable strategies for mass production of flexible electronics compatible with, for example, medical applications.<sup>10–12</sup>

Past theoretical studies have focused on the issue of what happens as a liquid bridge breaks and the solution of the Navier-Stokes equations diverges. An example of this can be seen in the classic work of Rayleigh and Plateau who used stability analysis to predict the breakup of liquid jets.<sup>13,14</sup> These analyses were later extended to liquid jets immersed in another liquid,<sup>15</sup> and to liquid jets extending at a constant rate.<sup>16</sup> More recent work has looked at systems where gravity can be neglected,<sup>17</sup> or have relied on perturbation methods to study solutions close to the static stability limit. Additional studies have focused on the formation of satellite drops,<sup>18</sup> or have investigated the effects of liquid inertia and viscosity in detail.<sup>19,20</sup> Self-similarity solutions have been the method of choice for analytical scaling studies of the pinching of liquid bridges.<sup>21</sup> This approach has been applied to both Newtonian<sup>22</sup> and non-Newtonian<sup>23–26</sup> liquids. Other analytical tools that have been used to study liquid bridges include lubrication theory—applied in the context of gravure-cell emptying,<sup>27,28</sup> boundary integral methods for study of the breakup of

extensional deformations,<sup>29</sup> and the solution of the Laplace-Young equation to study meniscus shapes, their mean curvatures, and the capillary forces that arise in such systems.<sup>30</sup>

A common goal from an engineering perspective is to achieve control over film shape and ink transfer onto the substrate, and to do so at large processing speeds. In coating applications, for example, it is important that the liquid drops from the gravure cells coalesce into a smooth film. Experimental studies of gravure coating have therefore sought to prevent ribbing<sup>31</sup> and air entrapment,<sup>32</sup> and to control film thickness.<sup>33–35</sup> In the case of gravure printing, the focus of past work has been to maximize ink transfer. This is important for several reasons. Not only are inks expensive, but residual ink in gravure cells can evaporate and leave behind solid residues that, with time, will deteriorate printing quality. Ink transfer also affects printing resolution.<sup>36</sup>

While focusing on the application of printing traditional nonconducting inks, past experimental and simulation work has sought to explore a wide range of parameters.<sup>37</sup> Some of the variables considered in the past have included the capillary number, inertia, contact angle, and variations in gravure cell geometry.<sup>38–42</sup> Other important considerations have included whether the contact line is allowed to slip or not,<sup>43,44</sup> and whether the shear between the gravure cell and the substrate is taken into account.<sup>45</sup> To visually observe the influence of these different parameters on ink transfer and gravure cell emptying, these earlier experiments have generally been performed at length scales that are significantly larger than those employed in actual applications.<sup>36,46,47</sup> However, as shown in

Correspondence concerning this article should be addressed to J. de Pablo at depablo@uchicago.edu.

this work, it is important to bear in mind the changes in the flow regimes that arise during scale up.

Past simulations of free surface flows have been implemented using mesh-based surface tracking<sup>43</sup> and volume of fluid (VOF)<sup>40</sup> techniques. The advantage of mesh-based surface tracking is that the exact location of the interface is known. A disadvantage is that topological changes are more difficult to support, so a simulation can typically only run until right before pinch-off of the liquid bridge.<sup>48</sup> By contrast, VOF relies on a smooth interface. This has the disadvantage that the surface normal and curvature are only known implicitly, which can lead to inaccurate interface curvature and spurious currents.<sup>49</sup> The advantages of the VOF method include mass conservation by construction (compared to level set methods),<sup>49</sup> and the ease with which topological changes, such as liquid-bridge breakup, and formation of satellite droplets, can be handled.

A majority of past liquid-bridge simulations have been performed in one-dimension (1-D) or two-dimensions (2-D),<sup>37,41–44,50–52</sup> although several three-dimensional (3-D) simulations have also been presented.<sup>53–57</sup> A comparison of 1-D and 2-D simulations<sup>58</sup> concluded that 1-D systems provide a good approximation for a 2-D system at low capillary numbers. A comparison of 2-D with 3-D simulations<sup>27</sup> found significant differences in ink transfer, due to ink getting trapped in the corners and edges of 3-D gravure cells, which did not happen in 2-D. While almost all simulations have been fully time dependent, a quasi steady-state approach using energy minimization to compute the shape of the interface of a droplet between two flat plates has also been proposed.<sup>59</sup>

One of the open questions in the field is what happens after the breakup of a liquid bridge.<sup>12</sup> A smooth interface method such as VOF is very well suited to address this question, and, to our knowledge, there is no precedent for direct visual comparison of experiments and VOF simulations involving non-Newtonian inks having realistic characteristics. In this work, we present this comparison between direct visualization and VOF simulation of gravure printing using index-matched colloidal inks and explore both relevant experimental and production length scales. The transparent silica microparticle inks considered here serve as an excellent model for conductive silver inks, which are of broad interest for the large-scale fabrication of flexible electronics. Note that silica microparticle suspensions exhibit a viscoelastic response, with a characteristic shear yield stress and pronounced shear thinning behavior upon yielding. The influence of printing speed and drop size on the ability to accurately transfer ink during the printing process is then examined. To facilitate direct visualization, the ink transfer experiments are carried out using large ink drops ( $\approx 1$  mm in size). For comparison, simulations are also carried out for those drop sizes. However, having validated the models adopted here, predictions of simulations are then presented for a system having characteristic dimensions of interest for printed electronics applications (i.e., 10  $\mu$ m in size).

Our simulations use the VOF method to resolve the ink and the surrounding gas phase; a remeshing technique is used to accommodate for the topological changes in the mesh as it deforms. As alluded to earlier, simulations are performed in 3-D, using a Ostwald-de Waele power-law model<sup>60</sup> for the shear-thinning behavior of the ink and Brackbill et al.'s model for the surface tension.<sup>61</sup> The contact angle is kept constant, and contact-line slip is implemented implicitly through the

VOF approach. Our results indicate that such an approach provides a reasonable description of the inks. However, especially at low processing speeds, ink transfer is underpredicted. This is likely due to the presence of silica particles at the contact line causing it to pin. This issue of pinning and the presence of inhomogeneities (particles) at the contact line is beyond the scope of this work but, as pointed out in the literature, more research is clearly needed to elucidate the relation between contact angles and contact line velocity,<sup>12</sup> as well as the pinning and depinning behavior of contact lines.

## Theory

The VOF method<sup>62</sup> has been shown to provide a good description of different types of free-surface flows.<sup>49,63,64</sup> The VOF approach evolves around the definition of a parameter  $\alpha$  with the following properties

$$\alpha = \begin{cases} 0 & \text{in gas phase} \\ (0, 1) & \text{on interface} \\ 1 & \text{in liquid phase} \end{cases} \quad (1)$$

The evolution of  $\alpha$  is calculated using the following transport equation

$$\frac{\partial \alpha}{\partial t} + \mathbf{V} \cdot (\alpha \mathbf{v}) + \mathbf{V} \cdot (\alpha(1-\alpha)\mathbf{v}_{lg}) = 0 \quad (2)$$

where  $\mathbf{v} = \alpha \mathbf{v}_l + (1-\alpha)\mathbf{v}_g$  is the phase-averaged velocity, and  $\mathbf{v}_{lg} = \mathbf{v}_l - \mathbf{v}_g$  is the velocity difference between the liquid and the gas phase. This equation is equivalent to a material derivative, but rewritten to minimize numerical diffusion.<sup>65</sup>

The volume fraction is used to calculate phase-averaged densities, velocities, and viscosities, which are used in the momentum balance

$$\frac{\partial \rho \mathbf{v}}{\partial t} + \mathbf{V} \cdot (\rho \mathbf{v} \otimes \mathbf{v}) = -\nabla p + \mathbf{V} \cdot (\mu \nabla \mathbf{v}) + \rho \mathbf{g} - \mathbf{f}_{st} \quad (3)$$

and the continuity equation

$$\mathbf{V} \cdot \mathbf{v} = 0 \quad (4)$$

In the above equations,  $\rho$  is the density,  $\mathbf{v}$  is the velocity,  $t$  is time,  $p$  is pressure,  $\mu$  is the viscosity,  $\mathbf{g}$  is gravity,  $\mathbf{f}_{st}$  is the surface tension force, and  $\otimes$  is the dyadic product. The density  $\rho$ , velocity  $\mathbf{v}$ , and viscosity  $\mu$ , are all phase averaged using  $\alpha$ . To complete the VOF model, one must provide expressions for the surface tension force  $\mathbf{f}_{st}$ , the shear thinning viscosity of the ink  $\mu_l$ , and the relevant boundary conditions. The surface tension force is calculated using the expression<sup>61</sup>

$$\mathbf{f}_{st} = \sigma_{st} \kappa \mathbf{V} \alpha \quad (5)$$

where  $\sigma_{st}$  is the surface tension coefficient

$$\kappa = -(\mathbf{V} \cdot \mathbf{n}) \quad (6)$$

is the curvature of the interface, and

$$\mathbf{n} = \frac{\mathbf{V} \alpha}{|\mathbf{V} \alpha|} \quad (7)$$

is the normal of the interface.

Because of the shape of the experimentally measured shear thinning curve presented below, and because of the computational expenses associated with a fully viscoelastic model, an Ostwald-de Waele power law model is adopted for the ink

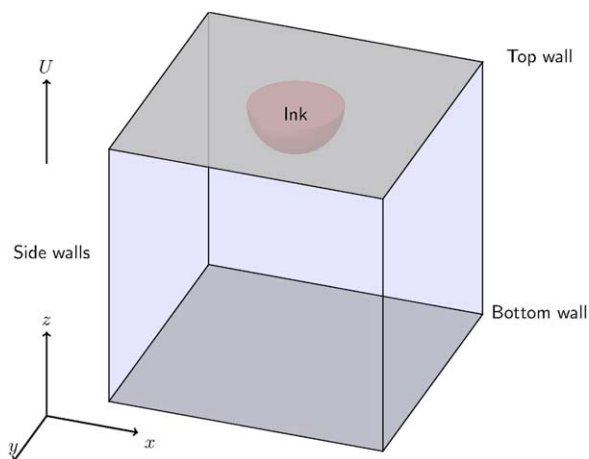


**Figure 1. Sketch of the computational domain used in the simulations.**

[Color figure can be viewed at [wileyonlinelibrary.com](http://wileyonlinelibrary.com).]

$$\mu_l = K \dot{\gamma}^{n-1} \quad (8)$$

where  $K$  is the flow consistency index,  $n$  the power law index, and  $\dot{\gamma}$  is the shear rate. The numerical implementation requires that a minimum and maximum viscosity be defined,  $\mu_{l,\min}$  and  $\mu_{l,\max}$ , at which the power law is cutoff. Note that we also tried to fit a Bird-Carreau model to the shear thinning curves, but the plateau viscosity does not span a large enough range to provide a good fit of our data.

As can be observed in Figure 1, the computational domain of the simulations consists of a box with the top wall moving upward. On the top and bottom walls, the boundary condition used for the velocity field is the no-slip condition. For mass conservation, the boundary condition for the pressure enforces both a zero flux and a zero second derivative of the pressure normal to the wall. A static contact angle is imposed for the VOF parameter,  $\alpha$ . Because the VOF method has a smooth interface, it does not require an explicit slip boundary condition. This results in an implicit slip length of the order of the grid size.<sup>66</sup>

Because the size of the box increases with time, gas is allowed to flow into the box through the side walls. For each grid cell next to the wall, the local inflow velocity is calculated from the wall-face normal component of the velocity vector associated with that specific grid cell. The total pressure  $p_0$  on the side walls is kept constant according to a simplified Bernoulli's equation

$$p_0 = p + \frac{1}{2} \rho |\mathbf{v}|^2 \quad (9)$$

The gas is assumed inviscid, and when the gas inflow velocity,  $\mathbf{v}$ , changes, the pressure,  $p$ , changes accordingly. The VOF parameter,  $\alpha$ , obeys a Dirichlet fixed value boundary condition on the side walls. The fixed value is set to zero, which is the equivalent of allowing only gas to flow in.

As initial conditions, both the velocity and pressure field are set to zero, and  $\alpha$  is set to form a cylinder with a  $1 \text{ mm}^3$  volume. When the simulation is started, the top plate is initially held in place so that the ink cylinder has time to equilibrate.

Mesh motion is accounted for using a Leibniz integral rule for higher dimensions (i.e., the Reynolds transport theorem), which states that for any vector field  $\mathbf{F}(\mathbf{x}, t)$

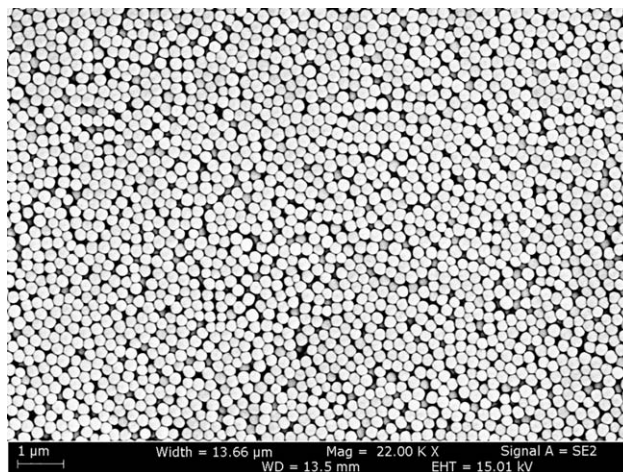


**Figure 2. SEM image of silica microparticles.**

$$\frac{d}{dt} \int_{D(t)} \mathbf{F}(\mathbf{x}, t) dV = \int_{D(t)} \frac{\partial}{\partial t} \mathbf{F}(\mathbf{x}, t) dV + \int_{\partial D(t)} \mathbf{F}(\mathbf{x}, t) \mathbf{v}_b \cdot \mathbf{n} dS \quad (10)$$

where  $\mathbf{v}_b$  is the velocity of the boundary of the mesh,  $V$  is the volume, and  $S$  is the surface. Using Gauss's theorem, this can be rewritten into

$$\frac{d}{dt} \int_{D(t)} \mathbf{F}(\mathbf{x}, t) dV = \int_{D(t)} \frac{\partial}{\partial t} \mathbf{F}(\mathbf{x}, t) dV + \int_{D(t)} \nabla \cdot (\mathbf{F}(\mathbf{x}, t) \mathbf{v}_b) dV \quad (11)$$

showing how the material derivative needs to be modified to implement moving boundaries.

## Methods

### Ink synthesis

Index-matched silica inks are prepared by first synthesizing silica microparticles, followed by index-matching in a water/dimethyl sulfoxide (DMSO) solution. An example of a batch of silica microparticles can be seen in Figure 2; their size distribution is shown in Figure 3. In a typical procedure, 100 mL tetraethyl orthosilicate is added into a mixed solution of ethanol (1200 mL) and water (600 mL). After stirring at room

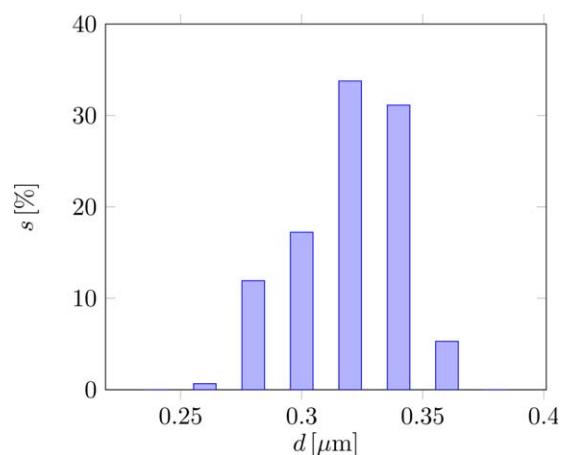


**Figure 3. The size distribution of the silica particles.**

$d$  is the particle diameter in  $\mu\text{m}$  and  $s$  is the fraction of particles with that size. [Color figure can be viewed at [wileyonlinelibrary.com](http://wileyonlinelibrary.com).]

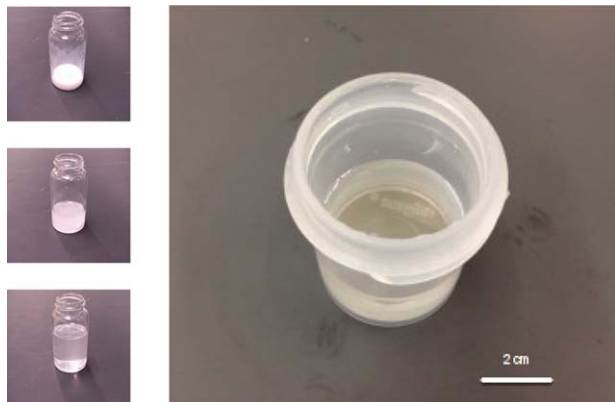


**Figure 4. Optical images of silica suspension of varying DMSO:H<sub>2</sub>O mixing ratio (left column) and an index-matched silica microparticle ink (right).**

The ratios are, from top to bottom, 0:100, 70:30, and 90:10 by weight. [Color figure can be viewed at [wileyonlinelibrary.com](http://wileyonlinelibrary.com).]

temperature for 30 min, 60 mL of ammonia solution (25 wt % in water) is added. A white silica suspension is obtained after stirring the solution for 10 h at room temperature. The resulting silica microparticles are then collected by centrifuging at 4000 rpm for 30 min, followed by dispersing them into 140 mL of water. The solution pH is then adjusted to 5.9 using a 8M HNO<sub>3</sub> solution. Following this, 0.4 g of polyethyleneimine (PEI, MW. 1300 g mol<sup>-1</sup>, 50 wt % in water) is added to the solution, and sonicated for 2 h to allow adsorption of PEI onto the silica surfaces. The resulting PEI-capped silica microparticles are then collected by centrifugation at 4000 rpm for 30 min. The opaque precipitates are then index-matched by adding DMSO until the suspension becomes transparent, as seen in Figure 4. The suspension is then concentrated by centrifuging at 4000 rpm for 30 min. The resulting precipitates are stiff. To make soft inks, an aliquot amount of polyvinylpyrrolidone (PVP, MW. 40,000 g mol<sup>-1</sup>) solution in DMSO:H<sub>2</sub>O (9.9:0.1 by wt) is added, and

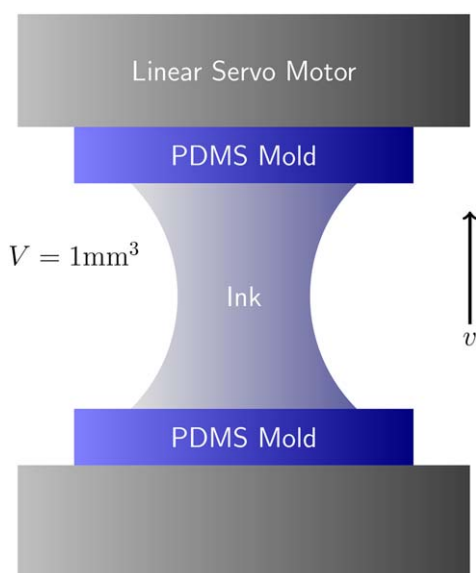


**Figure 5. Setup for ink transfer experiments.**

[Color figure can be viewed at [wileyonlinelibrary.com](http://wileyonlinelibrary.com).]

homogenized by a Thinky mixer at 2000 rpm for 30 min. An ink with a solids loading of 48 wt % with PVP/SiO<sub>2</sub> of 0.06 by wt is obtained. Three inks of varying solids loading (24, 37, 42 wt %) were prepared by diluting the 48 wt % ink using a mixed solution of DMSO:H<sub>2</sub>O (9.9:0.1 by wt).

### ***Ink transfer experiments***

A modified version of a capillary breakup rheometer was used in our experiments to simulate the ink transfer during the gravure printing process. Since this work is a fundamental study of the effect of printing speed and ink viscosity on the ink transfer process, the touchdown and shearing processes, which generally arise in actual roll-to-roll situations, are not taken into account. In addition, the ink is transferred between two flat plates, instead of from a gravure cell to a plate. The apparatus shown in Figure 5 consists of a linear servo motor to which a top plate, made by casting a mixture of Polydimethylsiloxane (PDMS) and crosslinker, is attached. The other plate is positioned underneath the upper plate, and is placed on an adjustable stage to control the position of the mold and line it up with the opposite plate. The contact angle made on each plate significantly influences ink transfer,<sup>41,46</sup> and PDMS has a good wettability for the samples considered here. As can be seen in Table 1, the contact angle remains nearly constant for the different inks. The advancing and receding contact angles and surface tensions were measured with a Kruss Drop Shape Analyzer. The equilibrium contact angle is calculated from the advancing and receding contact angles using the equations in Ref. 77. The size of the mold is 1 cm by 1 cm. During experiments,  $1 \pm 0.1 \text{ mm}^3$  of sample fluid was dropped on the bottom plate, and stretched vertically by the linear motor with a constant velocity ranging from 0.85 to  $73 \text{ mm s}^{-1}$ , as determined by tracking the position of the top plate over  $\sim 2.5 \text{ mm}$  of plate separation. An initial acceleration was only observed at the highest speed; the error in velocity is estimated to be  $\pm 5\%$ . Initially, there was a  $\sim 0.5 \text{ mm}$  gap between the top and bottom plate. All ink-transfer experiments were recorded with a Photron Fastcam APX 120K high-speed camera located at the side of the stage. Ink transfer was recorded at 60 - 2000 frames per second, depending on the velocity, and  $1024 \times 1024$  resolution. The residual ink volumes on the top and bottom plates were determined by weight measurements and analysis of visualization data using Image J and Pappus's centroid theorem. Both methods yielded similar results, but the image analysis method is preferred due to size of the drops and resolution of the microbalance ( $\pm 0.1 \text{ mg}$ ). At least three experiments were done at each condition. Fresh PDMS surfaces were used for every experiment.

### ***Ink transfer simulations***

The model outlined in the theory section is solved using the open source Computational Fluid Dynamics software package OpenFOAM 2.1.1.<sup>67,68</sup> Extensive benchmarking of the the OpenFOAM VOF solver can be found in literature.<sup>49</sup> An automated remeshing code was implemented to account for the large mesh deformation when the top plate moves away from the substrate.

The parameters describing the model were determined from shear thinning curves. The rheology data are shown in Figure 6. The same figure also shows the corresponding curve fits, which were used in our simulations. Table 2 shows the values of the parameters obtained from a Nonlinear Least Squares

**Table 1. Key Parameters of the Inks**

Sample	Solids Loading (%)	Density (kg m <sup>-3</sup> )	Surface Tension (N m <sup>-1</sup> )	Advancing Contact Angle (°)*	Receding Contact Angle (°)*	Equilibrium Contact Angle (°)**
1	24	1220 ± 12	0.0419 ± 0.0029	82.1 ± 2.7	68.7 ± 1.0	72.1
2	37	1278 ± 13	0.0444 ± 0.0044	84.2 ± 11	69.3 ± 1.9	74.2
3	42	1346 ± 8	0.0406 ± 0.0010	80.6 ± 5.5	67.6 ± 2.3	70.1

\*Measurement on PDMS.

\*\*Calculated from measured contact angles using expressions in Ref 77.

fit.<sup>69</sup> Parameters  $\mu_{\min}$  and  $\mu_{\max}$  denote the minimum and maximum cutoff viscosities, respectively. The maximum viscosity is important when using a power law model, because the viscosity is not defined at zero shear rate. The values of the equilibrium contact angles in Table 2 were used as the static contact angles in the simulations.

## Results and Discussion

### Dimensionless numbers

To determine which physics are important in the experiments, and which essential elements must be incorporated in simulations, it is helpful to introduce the following dimensionless numbers for this problem

$$Re = \frac{\rho LU}{K} \left( \frac{L}{U} \right)^{n-1} \quad (12)$$

$$Ca = \frac{KU}{\sigma_{st}} \left( \frac{U}{L} \right)^{n-1} \quad (13)$$

$$Bo = \frac{\rho g L^2}{\sigma_{st}} \quad (14)$$

where  $Re$  is the Power-Law Reynolds number,  $Ca$  is the Power-Law Capillary number, and  $Bo$  is the Bond number. These dimensionless numbers depend on  $U$ , the characteristic velocity,  $L$ , the characteristic length scale,  $\rho$ , the density,  $\sigma_{st}$ , surface tension,  $g$ , gravity,  $K$ , the flow consistency index, and  $n$ , the flow behavior index. The shear rate is approximated as  $U/L$ . Another dimensionless numbers commonly used in literature is the Ohnesorge number. However, it is omitted in this

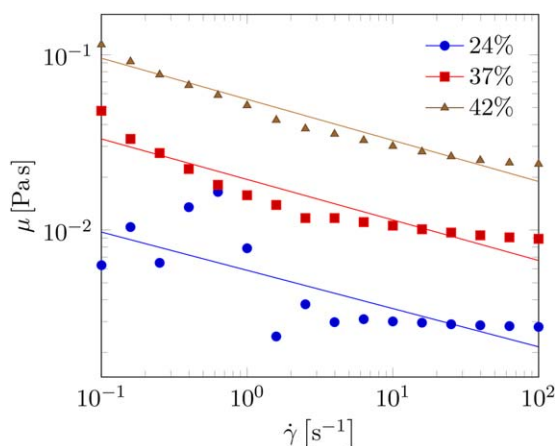


**Figure 6. Shear-thinning curves of index-matched silica microparticle inks of varying solids loading.**

The solid lines correspond to the Ostwald-de Waele power law model used in the simulations. [Color figure can be viewed at [wileyonlinelibrary.com](http://wileyonlinelibrary.com).]

analysis because it is independent of velocity, which is one of the parameter under investigation in this study.

In Figures 7 and 8, these three dimensionless numbers are plotted as a function of velocity for  $L \approx 1$  mm and  $L \approx 10$   $\mu$ m, respectively. The material properties of ink sample 3 are used in the plots, but the dimensionless numbers for the other two inks exhibit a similar behavior. Because geometry dependent prefactors are omitted, the absolute values of these numbers must be interpreted with caution. The graphs, however, reveal several interesting trends.

As velocity increases, the Reynolds number becomes larger, and thus inertial forces become more important relative to viscous forces. The Capillary number also increases, indicating that viscous forces become more dominant relative to surface tension. Comparing the value of the Reynolds number between Figures 7 and 8, viscous forces become more dominant over inertia at the  $L \approx 10$   $\mu$ m length scale; comparing the value of the Capillary number between the two figures, one sees that capillary forces become more dominant compared to viscous forces. Considering the much higher curvature of ink droplets at small length scales, surface tension effects are dominant in the  $L \approx 10$   $\mu$ m regime, as expected.

The Bond number is constant in both graphs, but it is much larger for Figure 7 than for Figure 8, suggesting that gravity cannot be neglected at the  $L \approx 1$  mm length scale but has a much smaller effect at the 10  $\mu$ m length scale. The Bond number crosses the Reynolds number line in Figure 7, indicating that in 1 mm gravure cells gravity is less important at higher velocities than at low velocities.

### Ink transfer experiments

To be consistent with literature reports,<sup>40,41,70,71</sup> the moving plate is labeled as the target for ink transfer. Figure 9 shows the transfer for different inks as a function of processing speed. For all velocities, transfer amounts are independent of the solids concentration of the ink, within the error of the measurement. Ink transfer generally increases with the velocity of the top plate, reaching  $\sim 45\%$  at the highest velocity (73 mm/s). It is difficult to anticipate whether the transfer amount will increase at higher processing speeds, which unfortunately are not accessible within our experimental setup.

For the lower velocities, past reports have found that ink transfer decreases as printing speed is increased.<sup>41,70,71</sup> In contrast, our experiments show the opposite behavior for all inks. The above analysis of the dimensionless numbers of this system provides a possible explanation. At the  $L=1$  mm length scale, the Bond number is dominant at slow printing speeds and the Reynolds number is dominant at high processing speeds. Because gravity acts against the direction of ink transfer, the transition from gravity-dominated flow at low speeds to inertia-dominated flow at high speeds could explain the suppressed ink transfer that is reported at low processing speeds. This is in agreement with the work of Khandavalli et al.,<sup>72</sup>

**Table 2. Fitting Parameters for the Inks Using the Ostwald-de Waele Power Law Model**

Sample	$k$ (Pa s <sup><i>n</i></sup> )	$n$	$\mu_{\min}$ (Pa s)	$\mu_{\max}$ (Pa s)
1	0.005890 ± 0.000721	0.781729 ± 0.050694	1.9 × 10 <sup>-7</sup>	0.0187
2	0.01944 ± 0.00104	0.76873 ± 0.02194	1.9 × 10 <sup>-7</sup>	0.0662
3	0.055725 ± 0.013800	0.765492 ± 0.013800	1.9 × 10 <sup>-7</sup>	0.193

who found that gravity enhancement can have a substantial effect on liquid pick-up from a gravure cell. Simulations, on the other hand, have typically set gravity to zero.

Figures 10 and 11 show different time series of the images captured by the high-speed camera. Looking closely at these images reveals static contact angle hysteresis and pinning of the contact line. This can have a significant influence on small-scale viscous free surface flows in general,<sup>73</sup> and on ink transfer<sup>74,75</sup> in particular. The observed contact line pinning is generally stronger for large velocities. Pinning at large velocities is consistent with literature reports. It has been found that at large Capillary numbers the velocity of the plate is so much larger than the velocity of the contact line that the contact line can be considered pinned.<sup>44</sup> The pinning could be affected by the silica particles. It is known from the literature that at large enough concentrations particles can cause the contact line to pin.<sup>76</sup> This would also be relevant to real conducting inks, because they typically include small metal particles.

**Ink transfer simulations**

Figure 12 shows results from simulations of ink transfer. Consistent with experiments all inks show similar ink transfer. The trend of increasing ink transfer which occurs in going from a processing speed of 0.9 to 9 mm s<sup>-1</sup> is predicted correctly. However, simulations underpredict the extent of ink transfer. This deviation can be attributed to the contact line pinning observed in experiments, which results in a larger ink transfer. Another explanation, which could have more important effects at larger speeds, is that the inks exhibit viscoelastic characteristics, which cannot be captured with a simple power-law model.

Figures 13 and 14 show the time series of the simulations for the velocities of 9 and 300 mm s<sup>-1</sup>. Overall, the simulations and experiments appear to agree. However, as mentioned above, in a number of cases the contact line in the experiments is pinned and does not move. This phenomenon is not captured by our simulations. This means that in the experiments the contact angle becomes smaller with time, while in the simulations the contact angle stays constant. When there is a difference in wettability between the two surfaces, this can have a large effect on ink transfer.<sup>44</sup> However, since in our work the wettability is the same for both surfaces, ink transfer goes to around 50% for both simulation and experiment at large processing speeds. As was shown in the experimental time series above, there was significant pinning compared to the other inks, probably due to the larger solids loading, which works against the effect of gravity.

Note that the reason that contact line pinning is not incorporated in our model is that there is no consensus on how to accurately describe contact line pinning and depinning due to surface chemistry inhomogeneities, surface roughness, and particles at the contact line. Another potential issue is caused by the fact that, as mentioned above, the contact line slip length for the VOF method is on the order of the grid size, which is about 1 × 10<sup>-7</sup> m. This could cause the contact line to move too fast. A more realistic slip length would be on the order of 1 × 10<sup>-9</sup> m, but having such a high resolution mesh to reduce the slip length, would make the simulations unacceptably slow. While the overall agreement of our predictions with experiment is satisfactory, our results for low velocities and high particle loadings suggest that to properly describe ink transfer for realistic inks a more sophisticated contact angle model needs to be implemented that not only correctly

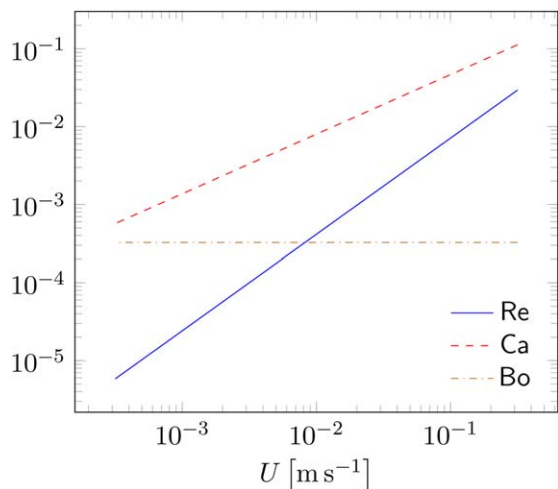


**Figure 7. The Power-Law Reynolds, Capillary, and Bond number for ink 3 as function of the processing velocity for  $L \approx 1$  mm.**

[Color figure can be viewed at [wileyonlinelibrary.com](http://wileyonlinelibrary.com).]

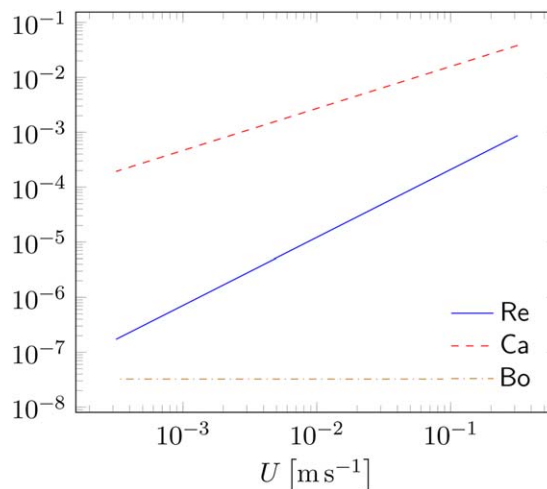


**Figure 8. The Power-Law Reynolds, Capillary, and Bond number for ink 3 as function of the processing velocity for  $L \approx 10$  μm.**

[Color figure can be viewed at [wileyonlinelibrary.com](http://wileyonlinelibrary.com).]

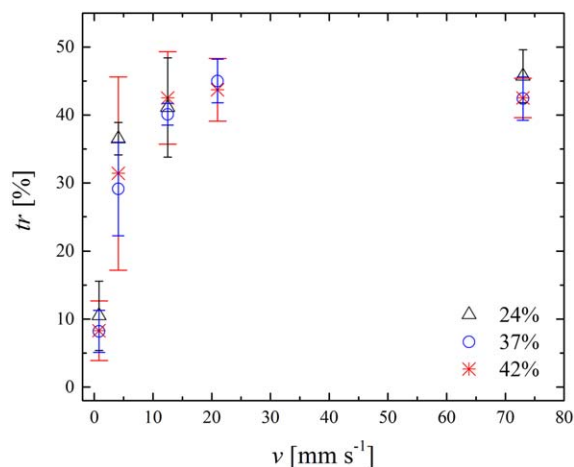


**Figure 9. Fraction of ink transfer from the bottom plate as a function of velocity. Results determined by analysis of visualization data. Error bars are the larger of (i) the 90% confidence interval calculated using results from 3-5 experiments or (ii) the characteristic measurement error based on image pixelation. Error in the velocity is  $\sim 5\%$  of reported value.**

[Color figure can be viewed at [wileyonlinelibrary.com](http://wileyonlinelibrary.com).]

describes the contact angle dependency on contact line velocity,<sup>12</sup> but that also predicts pinning and depinning of the contact line.

To explain the increased ink transfer that is observed at higher printing speeds, additional simulations without gravity

were performed on ink sample Number 3. The results are shown in Figure 15, where ink transfer is plotted as a function of the Capillary number, with and without gravity, at different length scales. Results for  $L \approx 1$  mm show that, as expected, gravity has a large impact on ink transfer at low speeds; at larger capillary numbers, however, results with and without gravity converge to the same answer.

While the asymmetry caused by gravity is not present in these simulations, and the contact angles on both the top and bottom plates are the same, the ink transfer ratio is not 50% for all processing speeds. This is consistent with literature reports,<sup>41</sup> and is most likely caused by the fact that the top plate accelerates very quickly when it starts moving, while the bottom plate is completely static. This sudden acceleration of only the top plate breaks the symmetry of the system. This seems to have a stronger effect at low speeds than at high speeds.

Having confirmed that the model provides a reasonable description of our experiments at 1 mm length scales, we now consider printing at the 10  $\mu\text{m}$  length scale for ink sample Number 3. The results are also shown in Figure 15. As also observed in the calculations without gravity, ink transfer is a lot larger at this length scale. Consistently with the dimensionless numbers analysis, this confirms that gravity has a lot smaller influence at this length scale, and shows how one has to be careful using experimental results at a large scale to make predictions about production environments at a small scale. In addition, it can be seen that without gravity, the curves for  $L \approx 1$  mm without gravity and  $L \approx 10$   $\mu\text{m}$  converge for higher capillary numbers, indicating that ink transfer scales with the capillary number in this regime. Because the smaller length scale corresponds to a smaller capillary number, ink transfer is found to increase, and our results are now consistent with literature.

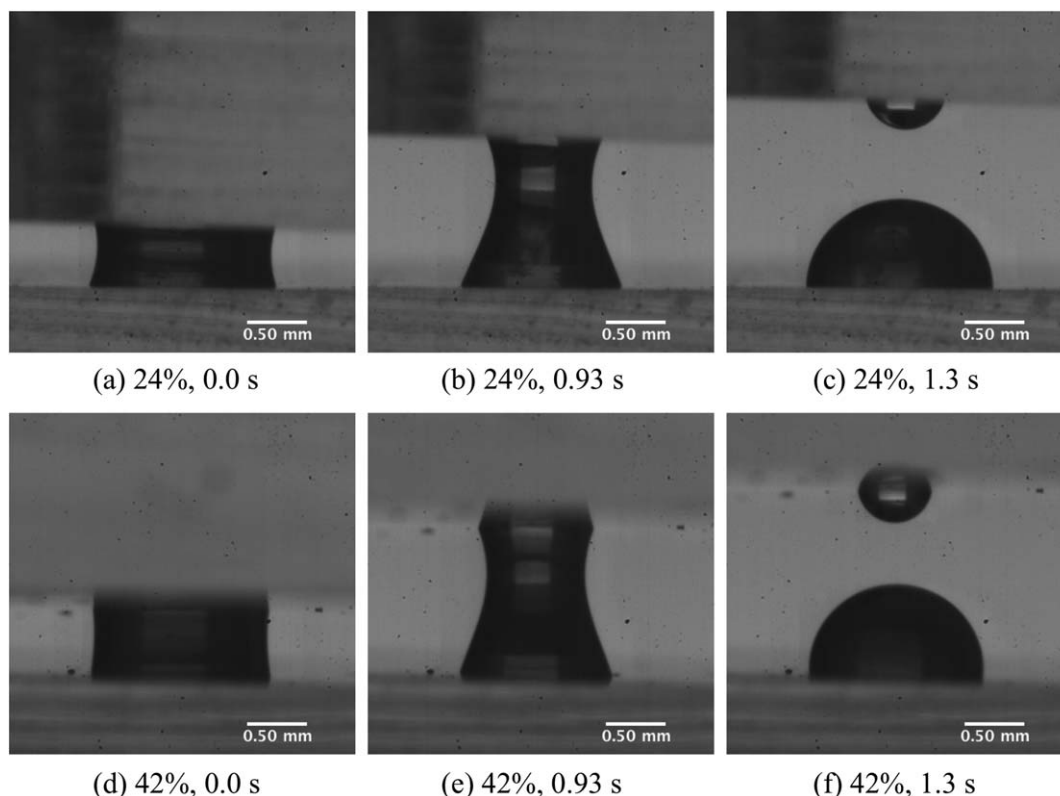


**Figure 10. Time series of images of 24% and 42% solids loading ink at  $0.82 \text{ mm s}^{-1}$ .**

(a) 24% ink, 0.0 s; (b) 24% ink, 0.93 s; (c) 24% ink, 1.3 s; (d) 42% ink, 0.0 s; (e) 42% ink, 0.93 s; (f) 42% ink, 1.3 s.

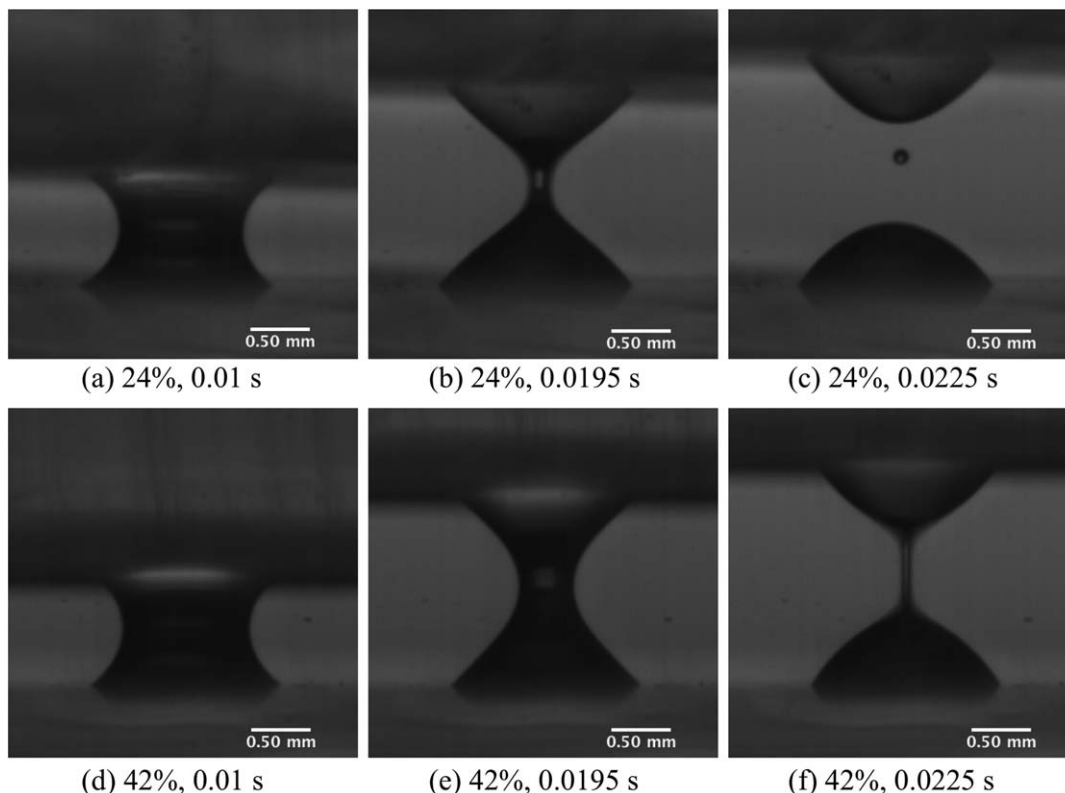


**Figure 11. Time series of images of 24% and 42% solids loading ink at  $73 \text{ mm s}^{-1}$ .**

(a) 24% ink, 0.01 s; (b) 24% ink, 0.0195 s; (c) 24% ink, 0.0225 s; (d) 42% ink, 0.01 s; (e) 42% ink, 0.0195 s; (f) 42% ink, 0.0225 s.

## Conclusions

Through advances in ink development and manufacturing technology, it is becoming increasingly clear that printed electronics are set to enter a wide array of commercial processes. To provide a foundation for studies of liquid bridges after breakup, and in order to provide engineering design rules that one may use for development of such processes, in this study we have presented a comparison of experiments and simulations of gravure printing for different, commercially relevant index matched silica particle inks. These inks were designed in such a way that surface tension and density are kept relatively constant for inks having different

concentrations of silica particles and different viscosities. These inks were then used in a series of gravure printing experiments in which ink transfer was measured as a function of processing speed. In general, ink transfer was found to be larger for higher processing speeds.

An analysis of the relevant dimensionless numbers indicates that as printing speed increases, the influence of gravity is reduced. A simulation without gravity confirmed this analysis, showing a strong difference in the results for low velocities, while showing convergence of the results for high velocities.

Comparison with simulation shows prediction of the trends for all inks, although for all inks the ink transfer was underpredicted. A possible explanation for the mismatch is that these inks exhibit a strong elastic behavior, which the power-law model adopted here is unable to capture. Another possible explanation is the contact line pinning observed in experiments, which was not accounted for in simulations and remains the subject of considerable debate. This pinning is probably caused by the large concentration of particles present in the ink. This suggests that in order to properly describe ink transfer for realistic, high-solids-loading inks, a contact angle model needs to be implemented that not only correctly describes the contact angle dependency on contact line velocity, but also correctly predicts the pinning and depinning of the contact line. Such models should also include an explicit representation of the particles, which is beyond the scope of this work.

Our analysis for gravure length scales compatible for flexible electronic printing processes ( $\approx 10 \mu\text{m}$ ) indicate that in this regime the effect of gravity is strongly reduced and that the ink transfer is dominated by capillary effects, resulting in higher ink transfer. More generally, our results indicate that simulations in terms of a relatively simple power-law model

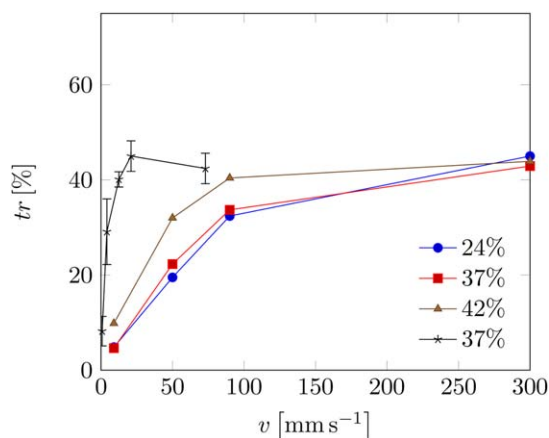


**Figure 12. Ink transfer fraction as function of printing speed as found in the simulations.**

The black curve is an experimental result, added for reference. [Color figure can be viewed at [wileyonlinelibrary.com](http://wileyonlinelibrary.com).]

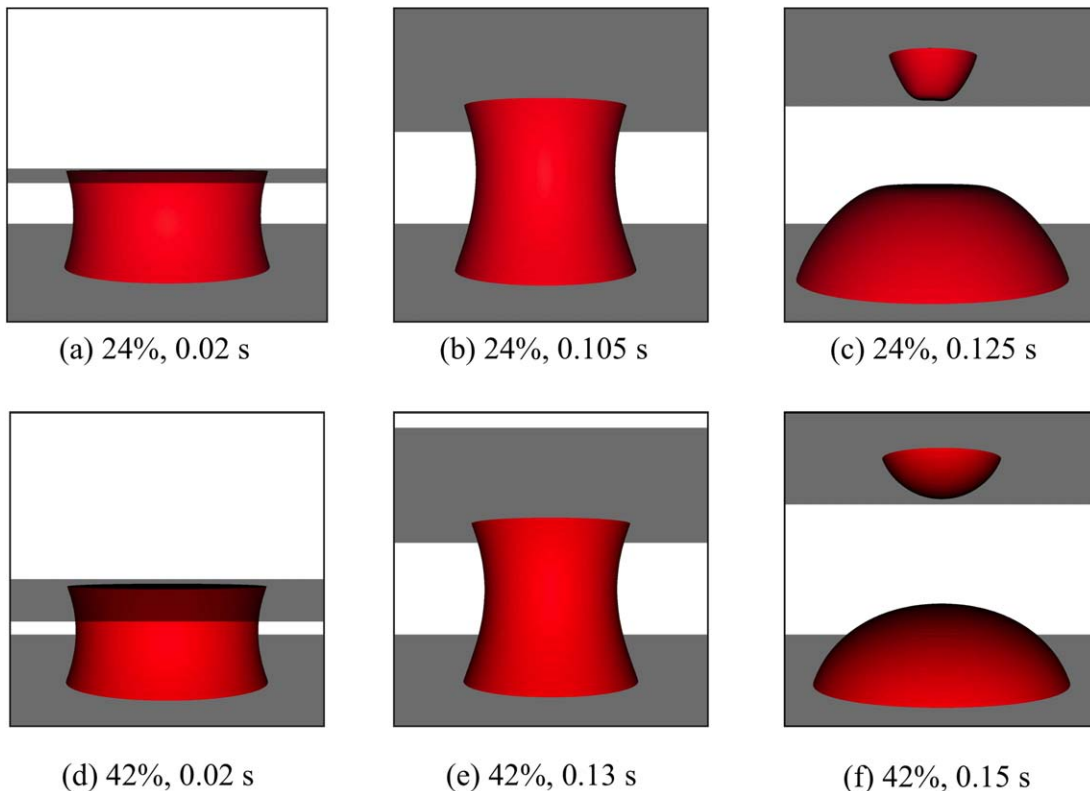


**Figure 13.** Time series of simulations of 24% and 42% solids loading ink at  $9 \text{ mm s}^{-1}$ .

(a) 24% ink, 0.02 s; (b) 24% ink, 0.105 s; (c) 24% ink, 0.125 s; (d) 42% ink, 0.02 s; (e) 42% ink, 0.13 s; (f) 42% ink, 0.15 s. [Color figure can be viewed at [wileyonlinelibrary.com](http://wileyonlinelibrary.com).]

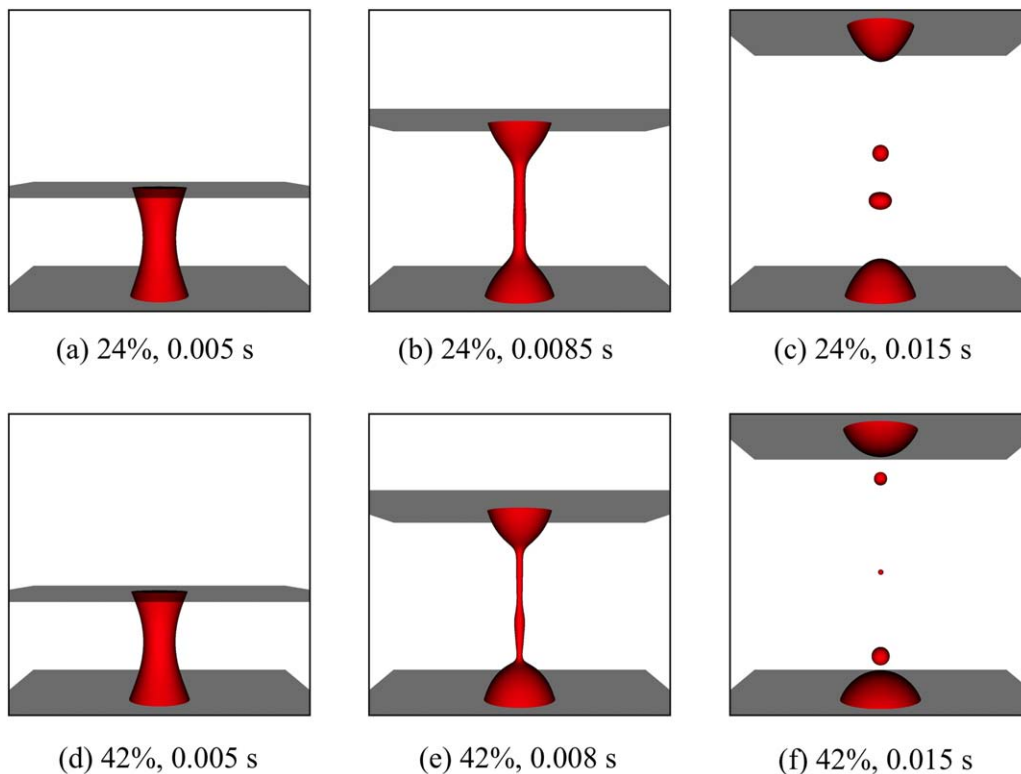


**Figure 14.** Time series of simulations of 24% and 42% solids loading ink at  $900 \text{ mm s}^{-1}$ .

(a) 24% ink, 0.005 s; (b) 24% ink, 0.0085 s; (c) 24% ink, 0.015 s; (d) 42% ink, 0.005 s; (e) 42% ink, 0.008 s; (f) 42% ink, 0.015 s. [Color figure can be viewed at [wileyonlinelibrary.com](http://wileyonlinelibrary.com).]

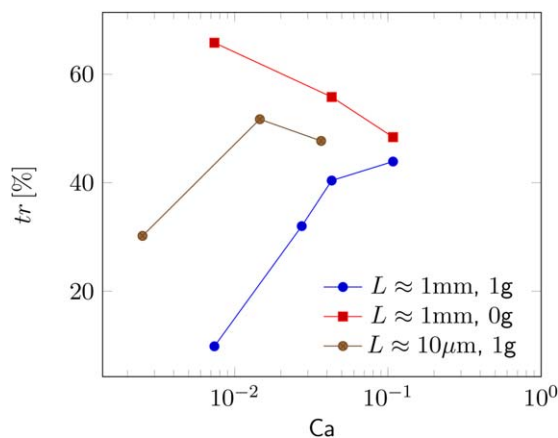


**Figure 15.** Ink transfer fraction as function of the Capillary number for ink sample 3 (42%), as found in the simulations.

[Color figure can be viewed at [wileyonlinelibrary.com](http://wileyonlinelibrary.com).]

are sufficient to predict ink transfer for different, realistic inks, and are thus a useful instrument for the design of production-relevant processes where visual experimental techniques are not readily available.

## Acknowledgements

This work was supported by a grant from the Multi-University Research Initiative (MURI) program - Office of Naval Research (MURI) - N00014-11-1-0690. The computational framework for calculation of fluid transfer was developed with support from the University of Chicago Materials research and Engineering Center (MRSEC), through grant DMR-1420709. The authors thank Wieslaw Suszynski, Krystopher Jochem, Noah Holzman, Shawn Dodds and Chung Hsaun Huang for assistance with experiments and data analysis.

## Literature Cited

- Eggers J. Nonlinear dynamics and breakup of free-surface flows. *Rev Mod Phys.* 1997;69:865.
- Oron A, Davis SH, Bankoff SG. Long-scale evolution of thin liquid films. *Rev Mod Phys.* 1997;69:931.
- Weinstein SJ, Ruschak KJ. Coating flows. *Annu Rev Fluid Mech.* 2004;36:29–53.
- Blake TD. The physics of moving wetting lines. *J Colloid Interface Sci.* 2006;299:1–13.
- Eggers J, Villermaux E. Physics of liquid jets. *Rep Prog Phys.* 2008;71:036601.
- Bonn D, Eggers J, Indekeu J, Meunier J, Rolley E. Wetting and spreading. *Rev Mod Phys.* 2009;81:739.
- Craster R, Matar O. Dynamics and stability of thin liquid films. *Rev Mod Phys.* 2009;81:1131.
- Stone HA. Interfaces: in fluid mechanics and across disciplines. *J Fluid Mech.* 2010;645:1–25.
- Basaran OA. Small-scale free surface flows with breakup: drop formation and emerging applications. *AIChE J.* 2002;48:1842–1848.
- Perelaer J, Smith PJ, Mager D, Soltman D, Volkman SK, Subramanian V, Korvink JG, Schubert US. Printed electronics: the challenges involved in printing devices, interconnects, and contacts based on inorganic materials. *J Mater Chem.* 2010;20:8446–8453.
- Krebs FC. Fabrication and processing of polymer solar cells: a review of printing and coating techniques. *Solar Energy Mater Solar Cells.* 2009;93:394–412.
- Kumar S. Liquid transfer in printing processes: liquid bridges with moving contact lines. *Annu Rev Fluid Mech.* 2015;47:67–94.
- Rayleigh L. On the instability of jets. *Proc R Soc London Ser A Math Phys Sci.* 1878;10:4–13.
- Plateau JAF. *Experimental and Theoretical Researches on the Figures of Equilibrium of a Liquid Mass Withdrawn from the Action of Gravity, etc.* Smithsonian Institution Press, Washington, DC. 1863.
- Tomotika S. On the instability of a cylindrical thread of a viscous liquid surrounded by another viscous fluid. *Proc R Soc London Ser A Math Phys Sci.* 1935;150:322–337.
- Tomotika S. Breaking up of a drop of viscous liquid immersed in another viscous fluid which is extending at a uniform rate. *Proc R Soc London Ser A Math Phys Sci.* 1936;153:302–318.
- Gillette R, Dyson D. Stability of fluid interfaces of revolution between equal solid circular plates. *Chem Eng J.* 1971;2:44–54.
- Tjahjadi M, Stone H, Ottino J. Satellite and subsatellite formation in capillary breakup. *J Fluid Mech.* 1992;243:297–317.
- Frankel I, Weihs D. Stability of a capillary jet with linearly increasing axial velocity (with application to shaped charges). *J Fluid Mech.* 1985;155:289–307.
- Frankel I, Weihs D. Influence of viscosity on the capillary instability of a stretching jet. *J Fluid Mech.* 1987;185:361–383.
- Eggers J. Universal pinching of 3 D axisymmetric free-surface flow. *Phys Rev Lett.* 1993;71:3458–3460.
- Papageorgiou DT. On the breakup of viscous liquid threads. *Phys Fluids.* 1995;7:1529–1544.
- Renardy M. Similarity solutions for jet breakup for various models of viscoelastic fluids. *J Non-Newtonian Fluid Mech.* 2002;104:65–74.
- Doshi P, Suryo R, Yildirim OE, McKinley GH, Basaran OA. Scaling in pinch-off of generalized Newtonian fluids. *J Non-Newtonian Fluid Mech.* 2003;113:1–27.
- Renardy M, Renardy Y. Similarity solutions for breakup of jets of power law fluids. *J Non-Newtonian Fluid Mech.* 2004;122:303–312.
- Suryo R, Basaran OA. Local dynamics during pinch-off of liquid threads of power law fluids: scaling analysis and self-similarity. *J Non-Newtonian Fluid Mech.* 2006;138:134–160.
- Schwartz L, Moussallp P, Campbell P, Eley R. Numerical modelling of liquid withdrawal from gravure cavities in coating operations. *Chem Eng Res Des.* 1998;76:22–28.
- Schwartz LW. Numerical modeling of liquid withdrawal from gravure cavities in coating operations; the effect of cell pattern. *J Eng Math.* 2002;42:243–253.
- Gaudet S, McKinley G, Stone H. Extensional deformation of Newtonian liquid bridges. *Phys Fluids.* 1996;8:2568–2579.
- Lian G, Thornton C, Adams MJ. A theoretical study of the liquid bridge forces between two rigid spherical bodies. *J Colloid Interface Sci.* 1993;161:138–147.
- Pulkrabek WW, Munter JD. Knurl roll design for stable rotogravure coating. *Chem Eng Sci.* 1983;38:1309–1314.
- Benkreira H, Cohu O. Direct forward gravure coating on unsupported web. *Chem Eng Sci.* 1998;53:1223–1231.
- Patel R, Benkreira H. Gravure roll coating of Newtonian liquids. *Chem Eng Sci.* 1991;46:751–756.
- Benkreira H, Patel R. Direct gravure roll coating. *Chem Eng Sci.* 1993;48:2329–2335.
- Kapur N. A parametric study of direct gravure coating. *Chem Eng Sci.* 2003;58:2875–2882.
- Yin X, Kumar S. Flow visualization of the liquid emptying process in scaled-up gravure grooves and cells. *Chem Eng Sci.* 2006;61:1146–1156.
- Zhang X, Padgett R, Basaran O. Nonlinear deformation and breakup of stretching liquid bridges. *J Fluid Mech.* 1996;329:207–245.
- Hoda N, Kumar S. Boundary integral simulations of liquid emptying from a model gravure cell. *Phys Fluids.* 2008;20:092106.
- Dodds S, Carvalho M, Kumar S. Stretching liquid bridges with moving contact lines: the role of inertia. *Phys Fluids.* 2011;23:092101.
- Huang W, Lee S, Sung H, Lee T, Kim D. Simulation of liquid transfer between separating walls for modeling micro-gravure-offset printing. *Int J Heat Fluid Flow.* 2008;29:1436–1446.
- Ahmed D, Sung H, Kim D. Simulation of non-Newtonian ink transfer between two separating plates for gravure-offset printing. *Int J Heat Fluid Flow.* 2011;32:298–307.
- Ghadiri F, Ahmed DH, Sung HJ, Shirani E. Non-Newtonian ink transfer in gravure-offset printing. *Int J Heat Fluid Flow.* 2011;32:308–317.
- Powell C, Savage M, Gaskell P. Modelling the meniscus evacuation problem in direct gravure coating. *Chem Eng Res Des.* 2000;78:61–67.

44. Dodds S, Carvalho MS, Kumar S. Stretching and slipping of liquid bridges near plates and cavities. *Phys Fluids*. 2009;21:092103.
45. Campana DM, Carvalho MS. Liquid transfer from single cavities to rotating rolls. *J Fluid Mech*. 2014;747:545–571.
46. Kang HW, Sung HJ, Lee TM, Kim DS, Kim CJ. Liquid transfer between two separating plates for micro-gravure-offset printing. *J Micromech Microeng*. 2009;19:015025.
47. Sankaran AK, Rothstein JP. Effect of viscoelasticity on liquid transfer during gravure printing. *J Non-Newtonian Fluid Mech*. 2012;175:64–75.
48. Basaran OA, Gao H, Bhat PP. Nonstandard inkjets. *Annu Rev Fluid Mech*. 2013;45:85–113.
49. Deshpande SS, Anumolu L, Trujillo MF. Evaluating the performance of the two-phase flow solver interFoam. *Comput Sci Discov*. 2012;5:014016.
50. Yao M, McKinley GH. Numerical simulation of extensional deformations of viscoelastic liquid bridges in filament stretching devices. *J Non-Newtonian Fluid Mech*. 1998;74:47–88.
51. Chung C, Kumar S. Emptying of viscoelastic liquids from model gravure cells. *J Non-Newtonian Fluid Mech*. 2015;221:1–8.
52. Lee JA, Rothstein JP, Pasquali M. Computational study of viscoelastic effects on liquid transfer during gravure printing. *J Non-Newtonian Fluid Mech*. 2013;199:1–11.
53. Cairncross RA, Schunk PR, Baer TA, Rao RR, Sackinger PA. A finite element method for free surface flows of incompressible fluids in three dimensions. Part I. Boundary fitted mesh motion. *Int J Numer Methods Fluids*. 2000;33:375–403.
54. Dimitrakopoulos P, Higdon J. On the displacement of fluid bridges from solid surfaces in viscous pressure-driven flows. *Phys Fluids*. 2003;15:3255.
55. Walkley M, Gaskell P, Jimack P, Kelmanson M, Summers J. Finite element simulation of three-dimensional free-surface flow problems with dynamic contact lines. *Int J Numer Methods Fluids*. 2005;47:1353–1359.
56. Xie X, Musson LC, Pasquali M. An isochoric domain deformation method for computing steady free surface flows with conserved volumes. *J Comput Phys*. 2007;226:398–413.
57. Zhou C, Yue P, Feng JJ, Ollivier-Gooch CF, Hu HH. 3D phase-field simulations of interfacial dynamics in Newtonian and viscoelastic fluids. *J Comput Phys*. 2010;229:498–511.
58. Yildirim OE, Basaran OA. Deformation and breakup of stretching bridges of Newtonian and shear-thinning liquids: comparison of one- and two-dimensional models. *Chem Eng Sci*. 2001;56:211–233.
59. Darhuber AA, Troian SM, Wagner S. Physical mechanisms governing pattern fidelity in microscale offset printing. *J Appl Phys*. 2001;90:3602–3609.
60. Ostwald W. Ueber die rechnerische darstellung des strukturgebietes der viskosität. *Kolloid Z*. 1929;47:176–187.
61. Brackbill J, Kothe D, Zemach C. A continuum method for modeling surface tension. *J Comput Phys*. 1992;100:335–354.
62. Hirt C, Nichols B. Volume of fluid (VOF) method for the dynamics of free boundaries. *J Comput Phys*. 1981;39:201–225.
63. Scardovelli R, Zaleski S. Direct numerical simulation of free-surface and interfacial flow. *Annu Rev Fluid Mech*. 1999;31:567–603.
64. Zhang X. Dynamics of drop formation in viscous flows. *Chem Eng Sci*. 1999;54:1759–1774.
65. Rusche H. *Computational Fluid Dynamics of Dispersed Two-Phase Flows at High Phase Fractions*. Ph.D. Thesis. Imperial College, London, UK, 2002.
66. Saha AA, Mitra SK. Effect of dynamic contact angle in a volume of fluid (VOF) model for a microfluidic capillary flow. *J Colloid Interface Sci*. 2009;339:461–480.
67. Jasak H. *Error Analysis and Estimation for the Finite Volume Method with Applications to Fluid Flows*. Ph.D. Thesis. Imperial College, London, UK, 1996.
68. The OpenFOAM Foundation Ltd London, UK. *OpenFOAM (Version 2.1.1) [Computer Software]*. 2011. Available at <http://openfoam.org/release/2-1-1/>. Accessed July 5, 2016.
69. R Core Team. *R: A Language and Environment for Statistical Computing*. Vienna, Austria: R Foundation for Statistical Computing, 2013. Available at <http://www.R-project.org>. Last accessed April 12, 2013.
70. Darhuber A, Miller S, Troian S, Wagner S. Process simulation for contact print microlithography. In: *Technical Proceedings of the International Conference on Modeling and Simulation of Microsystems*. San Diego, Computational Publ., Boston, MA, 2000:28–31.
71. Powell C, Savage M, Guthrie J. Computational simulation of the printing of Newtonian liquid from a trapezoidal cavity. *Int J Numer Methods Heat Fluid Flow*. 2002;12:338–355.
72. Khandavalli S, Lee JA, Pasquali M, Rothstein JP. The effect of shear-thickening on liquid transfer from an idealized gravure cell. *J Non-Newtonian Fluid Mech*. 2015;221:55–65.
73. Panditaratne JC. *Deflection of Microjets Induced by Asymmetric Heating and Related Free Surface Flows with Moving Contact Lines*. Ph.D. Thesis. Purdue University, West Lafayette, IN, 2003.
74. Dodds S, Carvalho MS, Kumar S. The dynamics of three-dimensional liquid bridges with pinned and moving contact lines. *J Fluid Mech*. 2012;1:1–20.
75. Chen H, Tang T, Amirfazli A. Liquid transfer mechanism between two surfaces and the role of contact angles. *Soft Matter*. 2014;10(15):2503–2507.
76. Deegan RD, Bakajin O, Dupont TF, Huber G, Nagel SR, Witten TA. Contact line deposits in an evaporating drop. *Phys Rev E*. 2000;62:756.
77. Tadmor K. Line energy and the relation between advancing, receding, and Young contact angles. *Langmuir* 2004;20:7659–7664.

Manuscript received July 24, 2015, and revision received Mar. 11, 2016.